The Higgs boson with the ATLAS experiment at the LHC: Discovery, measurement, and searches for new physics

A DISSERTATION PRESENTED
BY
TOMO LAZOVICH
TO
THE DEPARTMENT OF PHYSICS

IN PARTIAL FULFILLMENT OF THE REQUIREMENTS
FOR THE DEGREE OF
DOCTOR OF PHILOSOPHY
IN THE SUBJECT OF
PHYSICS

HARVARD UNIVERSITY
CAMBRIDGE, MASSACHUSETTS
MAY 2016

Thesis advisor: Professor Joao Guimaraes da Costa and Melissa Franklin   Tomo Lazovich

The Higgs boson with the ATLAS experiment at the LHC: Discovery, measurement, and searches for new physics

ABSTRACT

We measured things. And searched for other things. Here is what we found, please let me graduate.

Contents

Listing of figures

Listing of tables

THIS IS THE DEDICATION.

Acknowledgments

Lorem ipsum dolor sit amet, consectetuer adipiscing elit. Morbi commodo, ipsum sed pharetra gravida, orci magna rhoncus neque, id pulvinar odio lorem non turpis. Nullam sit amet enim. Suspendisse id velit vitae ligula volutpat condimentum. Aliquam erat volutpat. Sed quis velit. Nulla facilisi. Nulla libero. Vivamus pharetra posuere sapien. Nam consectetuer. Sed aliquam, nunc eget euismod ullamcorper, lectus nunc ullamcorper orci, fermentum bibendum enim nibh eget ipsum. Donec porttitor ligula eu dolor. Maecenas vitae nulla consequat libero cursus venenatis. Nam magna enim, accumsan eu, blandit sed, blandit a, eros.

0

Introduction

Part I

Preliminaries

1

The Standard Model and beyond: a theoretical overview

2

The ATLAS detector and the Large Hadron Collider

Part II

Observation and measurement of Higgs boson decays to $WW*$ with the ATLAS detector in LHC Run I at $\sqrt{s} = 7$ and 8 TeV

3

$H \rightarrow WW^* \rightarrow \ell\nu\ell\nu$ Analysis Strategy

3.1 Introduction

This chapter will present an overview of the strategy for searching for a Higgs boson in the $H \rightarrow WW^* \rightarrow \ell\nu\ell\nu$ decay topology. Its purpose is to present in broad terms how the search and measurement are undertaken, before going into details on the specific sub-categories within the broader analysis.

First, the topology of the signal final state and corresponding backgrounds are presented. Next, an overview of the variables used to reduce the backgrounds and enhance the signal is given. These will be described in general, while specific values of selection cuts and background estimation will be provided in subsequent chapters. Finally, the parameters of interest in the search and measurement will be defined, and a brief overview of the statistical treatment of the final Higgs candidates is shown.

Figure 3.1: A cartoon of the WW final state. Momenta are represented with thin arrows, spins with thick arrows. [2]

3.2 SIGNAL TOPOLOGY

The analysis presented here and in subsequent chapters is the study of the Higgs boson in the WW final state, where each W boson subsequently decays into a charged lepton and a neutrino. In its simplest form, the final state will then consist of two neutrinos and two charged leptons, each of which can be either an electron or a muon. If one or both of the Ws decay to τ leptons, only leptonic decays of the τ are considered, leading to additional neutrinos in the final state but still giving two charged leptons as before. Neutrinos are not detected in ATLAS, so the final state ultimately consists of two reconstructed leptons and missing transverse momentum (denoted as $E_{\mathrm{T}}^{\mathrm{miss}}$). Final states where both of the charged leptons are electrons or muons are referred to as the "same flavor" final states, while those with one electron and one muon are referred to as "different flavor".

The final state leptons will also exhibit unique correlations due to the fact that they are arising from the decay of a spin zero resonance. In particular, the spins of the final state leptons and neutrinos must all cancel, as shown in figure 3.1. Because the neutrino has a left handed helicity and the anti-neutrino has a right handed helicity, the spin and momentum of the particles will be anti-aligned and aligned, respectively. In the transverse plane, the momenta of all four final state objects must cancel as well. With the constraint of having both the momenta and the spin alignments cancel, the final state kinematics strongly prefer having a small angle between the leptons in the transverse plane (low $\Delta\phi_{\ell\ell}$). This angular correlation will also lead to low values of the di-lepton invariant mass $m_{\ell\ell}$. These unique signal final state kinematic correlations will be exploited to define the ultimate signal region.

While the basic final state consists of two leptons and $E_{\mathrm{T}}^{\mathrm{miss}}$, there can be additional objects as well depending on the production mode of the Higgs. As described in detail in Chapter 1, if the Higgs is produced via vector boson fusion production, there will be two additional forward jets in the event. Even in gluon fusion, one or more jets can be produced through initial state radiation from the incoming gluons. The analysis is separated into different signal regions depending on the number of hard jets reconstructed in the final state as well.

3.3 Background processes

Many processes from the Standard Model can also produce a final state with two leptons and missing transverse momentum . This section lists the dominant backgrounds to Higgs production. It gives general descriptions of how the backgrounds mimic Higgs production and how they can be reduced. The details of background estimation and specific cuts are left for later sections. Table 3.1 summarizes the different processes.

3.3.1 Standard Model WW production
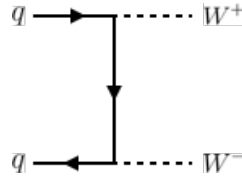
Figure 3.2: Feynman diagram for Standard Model WW production

Non-resonant Standard Model diboson production, as shown in figure 3.2, is an irreducible background to Higgs boson production in the WW final state. It produces the same exact final state objects, namely leptonically decaying W bosons. There are no additional objects in the final state that allow for background reduction. Therefore the analysis solely relies on the correlations between the leptons to reduce this background.

3.3.2 Top quark production

Production of top quarks, either in pairs ($t\bar{t}$ production) or singly (e.g. Wt production), can also mimic Higgs production. Because top quarks decay via $t \rightarrow Wb$, top pair production can produce a final state with two W bosons that then decay leptonically. In this case, however, there are two additional jets from the bottom quarks in the final state. This allows the analysis to veto on the presence of jets identified as originating from a b in order to reduce the size of the background.

Single top production can occur via s-channel, t-channel, or associated production (Wt). The mode which most closely resembles the Higgs final state is Wt. In this case, there are two real W bosons produced, as with $t\bar{t}$. However, the decay of the single top quark will still also produce one b-jet, meaning a b veto will reduce this background as well.

Figure 3.3 shows the Feynman diagrams for $t\bar{t}$ and Wt production.
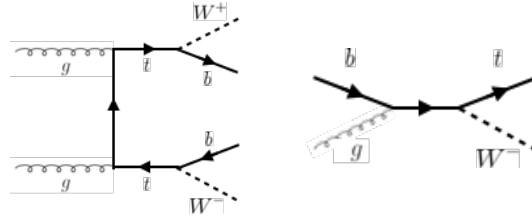
Figure 3.3: Feynman diagrams for top pair production (left) and Wt production (right)

3.3.3 W+jets background

Single W boson production, in association with jets, is a unique background. The other background considered so far have all included real leptons in the final state. In this case, however, only one real lepton from the decay of a W exists in the final state. The second reconstructed lepton can arise from two different cases. First, the lepton may truly be an algorithm "fake", or a jet misidentified as a lepton by either the electron or muon reconstruction algorithms. Second, the lepton may be a real lepton but coming from semi-leptonic decays of particles inside the shower of the jet. This background can be reduced by requiring that the reconstructed lepton have little activity surrounding it in the calorimeter (also known as an "isolated" lepton). Figure 3.4 shows the Feynman diagram for W+jets production.
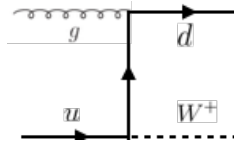
Figure 3.4: An example Feynman diagram of W+jets production

3.3.4 Z/γ^*+jets background

Production of a Z/γ^* in association with jets (also known as Drell-Yan) is also a background to Higgs production. In particular, the same flavor final states have a large Z+jets background, as the Z decays into two leptons of the same flavor. (This background also enters the different flavor final state through the leptonic decays of $Z \to \tau\tau$). Figure 3.5 shows the production of a Z in association with one jet. Because there are no neutrinos in this final state, variables like $E_{\mathrm{T}}^{\mathrm{miss}}$ can be used to reduce the background.
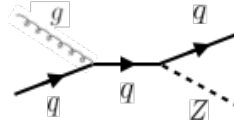
Figure 3.5: An example Feynman diagram of Z+jets production

3.3.5 Other (subdominant) backgrounds

THere are additional processes which contrinute to the background composition but are not produced as frequently as those listed already. The first of these are referred to as VV or "Other diboson" processes and include multiple Standard Model diboson processes, including WZ, ZZ, $W\gamma$, $W\gamma^*$, and $Z\gamma$ production. Additionally, there is background from QCD multijet production, where two jets are misidentified as leptons.

3.4 Isolating an $H \to WW^* \to \ell\nu\ell\nu$ signal

As presented in section 3.2, there are many different combinations of objects that can define a $H \to WW^* \to \ell\nu\ell\nu$ final state. The multiplicity of jets and the flavor combinations of the leptons both lead to a combinatorically large number of potential signal regions. Additionally, signal regions can be optimized separately to be sensitive to the distinct production modes of the Higgs. Gluon fusion, vector

Category	Process	Description
SM WW	$WW \to \ell\nu\ell\nu$	Real leptons and neutrinos
Top quark production	$t\bar{t} \to WbW\bar{b} \to \ell\nu b\ell\nu\bar{b}$	Real leptons, untagged bs
	$tW \to WbW \to \ell\nu\ell\nu b$	Real leptons, untagged b
	$t\bar{b}, tq\bar{b}$	Untagged b, jet misidentified as lepton
Drell-Yan	$Z/\gamma^* \to ee, \mu\mu$	"Fake" $E_{\mathrm{T}}^{\mathrm{miss}}$
	$Z/\gamma^* \to \tau\tau \to \ell\nu\nu\ell\nu\nu$	Real leptons and neutrinos
Other dibosons	$ZZ \to \ell\ell\nu\nu$	Real leptons and neutrinos
	$W\gamma^*, WZ \to \ell\nu\ell\ell, ZZ \to \ell\ell\ell\ell$	Unreconstructed leptons
	$W\gamma, Z\gamma$	γ reconstructed as e, unreconstructed lepton
W+jets	$Wj \to \ell\nu j$	Jet reconstructed as lepton
QCD multijet	jj	Jets reconstructed as leptons

Table 3.1: A summary of backgrounds to the $H \to WW^* \to \ell\nu\ell\nu$ signal

boson fusion, and associated production of a Higgs all lead to unique final state topologies. Figure 3.6 delineates the different signal regions used in the gluon fusion and vector boson fusion $H \to WW^*$ analyses. While there are different optimizations possible in each signal region, there are also some commonly shared selections that will be described here.

3.4.1 Event pre-selection

Before being sorted into the distinct signal regions, basic cuts are applied on the reconstructed objects in the event to select Higgs-like event candidates. First, two oppositely charged leptons are required. The p_{T} threshold on the leptons is a particularly important consideration for this signal. Because the second W produced in the decay can be off-shell, it tends to produce lower momentum leptons. Thus, being able to lower the p_{T} threshold while still maintaining a low background rate is critical. Figure 3.7 shows an example of the subleading lepton p_{T} for a VBF $H \to WW^*$ signal compared to the corresponding $t\bar{t}$ background. Note that the lepton p_{T} spectrum is considerably softer in the signal sample.

Once the leptons are selected, the last requirement for event pre-selection is the presence of neutrinos. As neutrinos cannot be detected directly in ATLAS, $E_{\mathrm{T}}^{\mathrm{miss}}$ can be used as a proxy for the combined neutrino momentum in the transverse plane. In general, it is expected that the signal should have a harder

Figure 3.6: An illustration of the unique analysis signal regions [2]
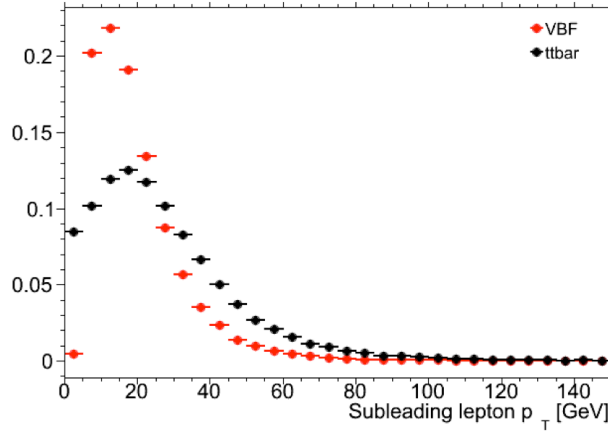
Figure 3.7: A comparison of the subleading lepton p_T spectrum between VBF $H \to WW^*$ production and $t\bar{t}$ background

E_T^{miss} spectrum than backgrounds, especially if those backgrounds did not contain neutrinos. One additional consideration when using E_T^{miss} is the fact that mis-measurements of objects in the detector can lead to imbalances in the transverse plane that are not due to real particles escaping the detector. One indicator that this is the case is that the E_T^{miss} vector in the transverse plane will be pointing in the

same direction as the mis-measured object. Therefore, a new variable, $E_{\mathrm{T,rel}}^{\mathrm{miss}}$, is used in the pre-selection. $E_{\mathrm{T,rel}}^{\mathrm{miss}}$ is defined in equation 3.1.

$$
E_{\mathrm{T,rel}}^{\mathrm{miss}} = \begin{cases} E_{\mathrm{T}}^{\mathrm{miss}} \ \sin \Delta\phi_{\mathrm{near}} & \text{if } \Delta\phi_{\mathrm{near}} < \pi/2 \\ E_{\mathrm{T}}^{\mathrm{miss}} & \text{otherwise,} \end{cases} \tag{3.1}
$$

If the closest object to the $E_{\mathrm{T}}^{\mathrm{miss}}$ vector is within $\pi/2$ radians in the transverse plane, the $E_{\mathrm{T}}^{\mathrm{miss}}$ is projected away from this object. Otherwise, the normal $E_{\mathrm{T}}^{\mathrm{miss}}$ vector is used. Figure 3.8 shows a graphical illustration of this concept.
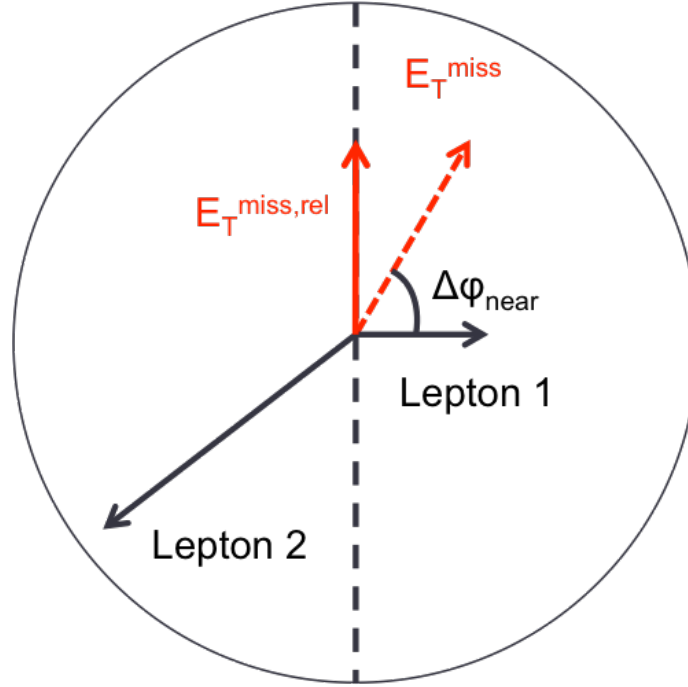
Figure 3.8: A graphical illustration of the $E_{\mathrm{T,rel}}^{\mathrm{miss}}$ calculation

Once both the lepton and $E_{\mathrm{T}}^{\mathrm{miss}}$ pre-selections are made, the analysis can be divided into different regions according to jet multiplicity.

3.4.2 JET MULTIPLICITY

Jet multiplicity, denoted as n_j, is used to sub-divide the analysis into its distinct signal regions. The reason for this is twofold. First, different jet multiplicity bins will be more or less sensitive to different Higgs

production modes. For example, the $n_j \geq 2$ region is more sensitive to VBF production because of the two hard jets produced at matrix element level. For gluon fusion production to enter this bin, two initial state radiation jets must be emitted. Second, background composition varies greatly in different bins of n_j. Figure 3.9 shows the jet multiplicity in both the different flavor and same flavor regions. It also shows the background composition in the bins of n_b. There are a few clear trends from this distribution. The first is that the Drell-Yan background dominates in the same flavor channels for $n_j \leq 1$. Second, the top background becomes a clear contributor to the total background for $n_j \geq 1$. Lastly, the SM WW production dominates in the $n_j = 0$ bin, as it is an irreducible background to $H \to WW^*$ production. Because of these distinct features, each jet multiplicity bin is treated separately.
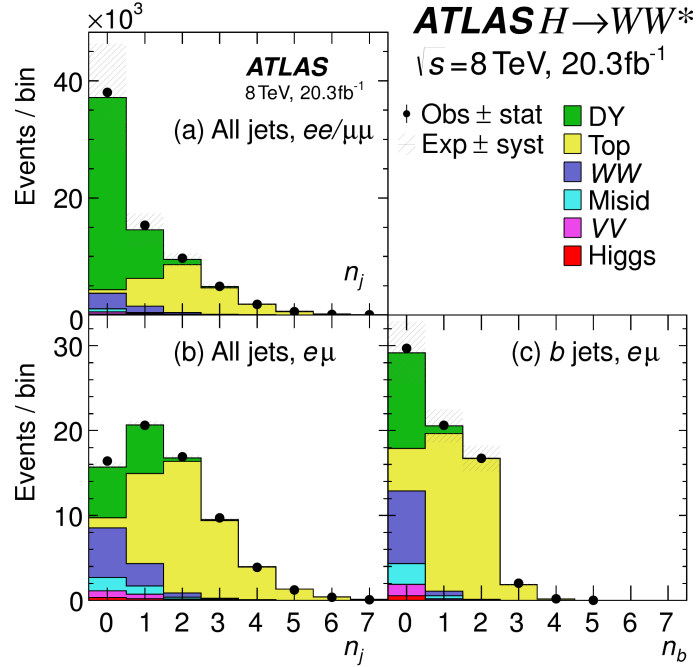
Figure 3.9: Predicted backgrounds (compared with data) as a function of n_j (a and b) and n_b (c)

3.5 BACKGROUND REDUCTION IN SAME-FLAVOR FINAL STATES

As described in section 3.4.2, the background composition of the same flavor final states is unique to that of the different flavor states. In particular, Drell Yan processes play a much larger role because the Z/γ^* decays to same flavor leptons. Because real neutrinos are absent in the Z/γ^* decays to ee and $\mu\mu$,

a cut on E_T^{miss} should largely reduce the background. However, as this section will demonstrate, with increasing pileup conditions the resolution of the calorimeter-based E_T^{miss} degrades greatly. Therefore, two new variables for Z/γ^* background reduction are constructed and described in this section.

3.5.1 Pileup and E_T^{miss} resolution

Secondary interactions of protons in the colliding bunches of the LHC (known as pileup interactions, described in detail in Chapter 2) deposit energy into the ATLAS calorimeter on top of the energy that comes from the hard scatter process that is being searched for or analyzed. The calculation of E_T^{miss} is fundamentally Poissonian, as summing up all of the energy deposits in individual calorimeter cells or clusters is similar to a counting experiment. Thus, the energy resolution scales as $\sqrt{E}$, just as the error on a mean of N in a Poisson distribution is $\sqrt{N}$. As more energy is deposited in the calorimter, the E_T^{miss} resolution degrades, meaning that the E_T^{miss} resolution is particularly sensitive to LHC instantaneous luminosity conditions.

Figure 3.10 shows an event display of a Z/γ^* + jets event candidate with the twenty-five reconstructed primary vertices. This display illustrates that while the interaction of interest only has tracks coming from the hardest primary vertex, all of the secondary interactions will deposit energy in the calorimeter as well.

Figure 3.11 shows the RMS of the E_T^{miss} distribution in $Z \rightarrow \mu\mu$ events (where there are no real neutrinos) as a function of the number of the average number of interactions. Under 2011 LHC conditions, this RMS was approximately 9 GeV, while under 2012 running conditions the resolution worsened to 12 GeV. This worsening dilutes the efficacy of a cut on E_T^{miss} to reduce the Z/γ^* background.

3.5.2 Track-based definitions of missing transverse momentum

Because the increasing number of secondary proton-proton interactions degrades calorimeter-based E_T^{miss} resolution, a new variable using only contributions from the primary interaction vertex is necessary to further reduce the Z/γ^* background. While it is not possible to associate calorimeter energy deposits with a particular vertex, individual charged particle tracks in the Inner Detector are associated to
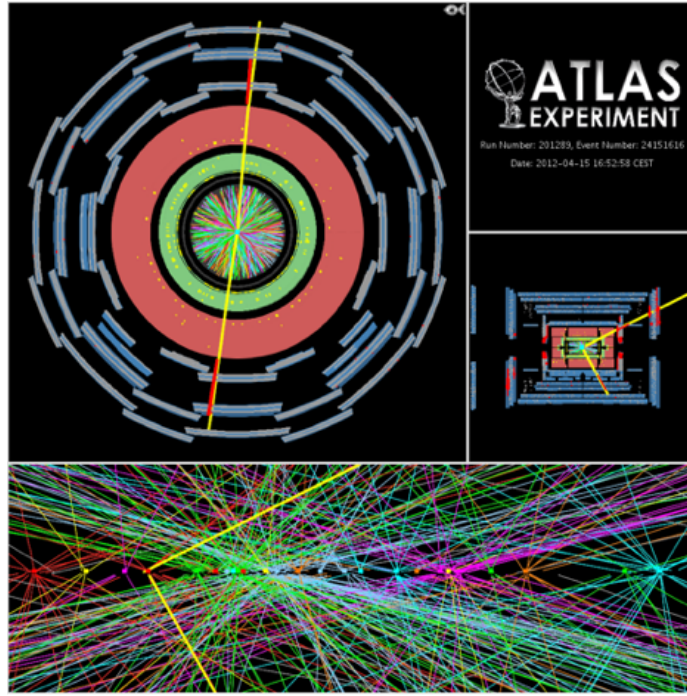
Figure 3.10: An event display of a Z/γ^* + jets event illustrating the effect of pileup interactions
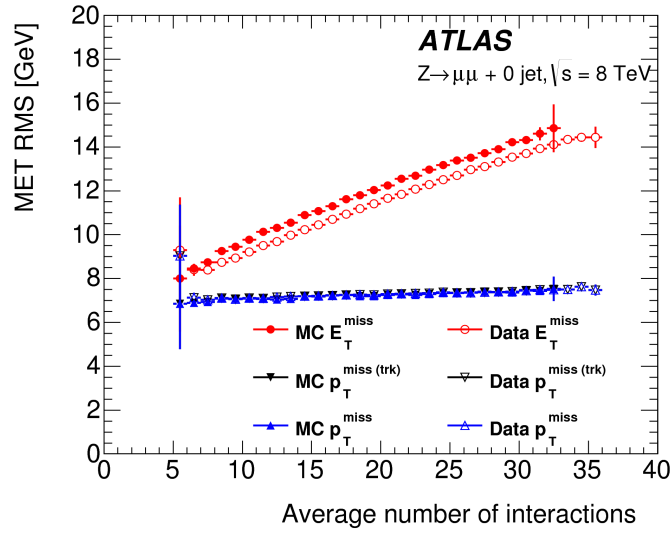
Figure 3.11: The RMS of different missing transverse momentum definitions as a function of the average number of interactions per bunch crossing

unique vertices. Thus, two track-based definitions of missing transverse momentum, using only tracks coming from the primary vertex in the event, are used in the analysis. The simplest variable, $p_{\mathrm{T}}^{\mathrm{miss\,(trk)}}$, is the vectorial sum of the p_{T} of all of the tracks in the event and the selected leptons (excluding the tracks

associated with the selected leptons to avoid double counting). This is defined in equation 3.2.

$$\boldsymbol{p}_{\mathrm{T}}^{\mathrm{miss\,(trk)}} = -\left(\sum_{\substack{\text{selected} \\ \text{leptons}}} \boldsymbol{p}_{\mathrm{T}} + \sum_{\substack{\text{other} \\ \text{tracks}}} \boldsymbol{p}_{\mathrm{T}} \right), \qquad (3.2)$$

In events with hard jets, a better resolution on the missing transverse momentum is obtained by including the calorimeter based measurement of the hard jets rather than the track based measurements. Thus, another variable, $p_{\mathrm{T}}^{\mathrm{miss}}$, is defined, using the nominal measurements of p_{T} for the selected leptons and jets and using tracks rather than calorimeter clusters for the soft component of the missing transverse momentum . This is defined in equation 3.3.

$$\boldsymbol{p}_{\mathrm{T}}^{\mathrm{miss}} = -\left(\sum_{\substack{\text{selected} \\ \text{leptons}}} \boldsymbol{p}_{\mathrm{T}} + \sum_{\substack{\text{selected} \\ \text{jets}}} \boldsymbol{p}_{\mathrm{T}} + \sum_{\substack{\text{other} \\ \text{tracks}}} \boldsymbol{p}_{\mathrm{T}} \right), \qquad (3.3)$$

Figure 3.11 illustrates that these two new variables accomplish their intended purpose. The resolution as a function of mean number of interactions for both $p_{\mathrm{T}}^{\mathrm{miss\,(trk)}}$ and $p_{\mathrm{T}}^{\mathrm{miss}}$ is much flatter compared to the dependence for $E_{\mathrm{T}}^{\mathrm{miss}}$.

Figure 3.12a shows the difference between the true and reconstructed values of missing transverse momentum using both the track-based $p_{\mathrm{T}}^{\mathrm{miss}}$ and calorimeter based $E_{\mathrm{T}}^{\mathrm{miss}}$. The RMS of the distribution improves by 3.5 GeVwhen using $p_{\mathrm{T}}^{\mathrm{miss}}$.

3.5.3 Distinguishing Z/γ^* +jets and $H \to WW^*$ topologies

The track-based definitions of missing transverse momentum were constructed to mitigate degrading performance as a function of pileup. However, an additional variable can be constructed to exploit kinematic and topological differences between the Z/γ^* background and $H \to WW^*$ signal. Because there are no real neutrinos in the final state (in the case of $Z/\gamma^* \to ee, \mu\mu$ decays), the dilepton system of a Z/γ^* will be balanced with the jets produced in the hard scatter. A new variable, f_{recoil}, is constructed to estimate the balance between the dilepton system and the jets in the quadrant opposite the dilepton vector in the transverse plane. It is defined in equation 3.4. The numerator of f_{recoil} is the magnitude of the vectorial sum of the p_{T} of jets in the quadrant opposite the dilepton system, weighted by each jet's Jet
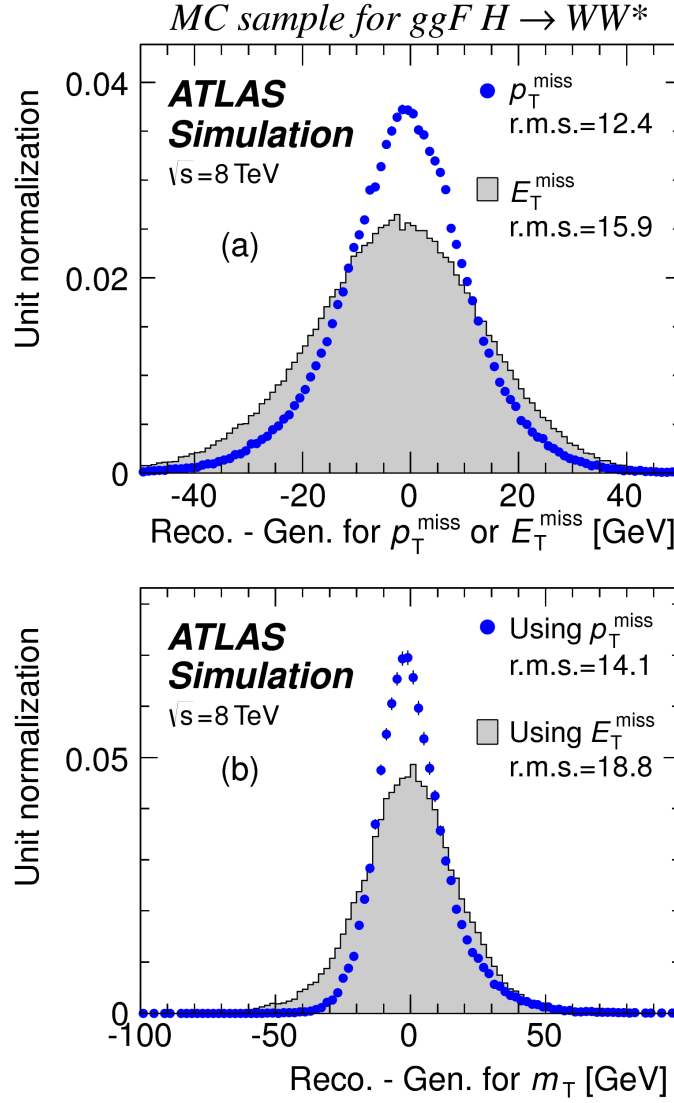
Figure 3.12: The difference between the true and reconstructed values of the missing transverse momentum (a) and m_T (b) in a gluon fusion signal sample

Vertex Fraction (JVF, described in chapter 2). The denominator is the magnitude of the dilepton p_T.

$$f_{\text{recoil}} = \left| \sum_{\text{jets } j \text{ in } \wedge} \text{JVF}_j \cdot \boldsymbol{p}_T^j \right| \bigg/ p_T^{\ell\ell}. \tag{3.4}$$

Figure 3.13 shows a shape comparison of the distribution of f_{recoil} in a simulated $Z/\gamma^* + \text{jets}$ sample, a $H \to WW^*$ signal sample, and other backgrounds that contain real neutrinos. The $Z/\gamma^* + \text{jets}$ events

tend to be more balanced between the dilepton system and recoiling jets, while the processes containing real neutrinos are less balanced in the transverse plane. Thus, a cut on f_recoil will also reduce the Z/γ^* + jets background while maintaining a good signal efficiency.

Figure 3.13: Comparison of f_recoil distributions for Z/γ^*+jets, $H \to WW^*$, and other backgrounds with real neutrinos.

3.5.4   Optimizing background reduction cuts

The cuts on $p_\text{T}^\text{miss (trk)}$ and f_recoil used to reduce the Z+jets background must be optimized to maximize their efficacy. Fi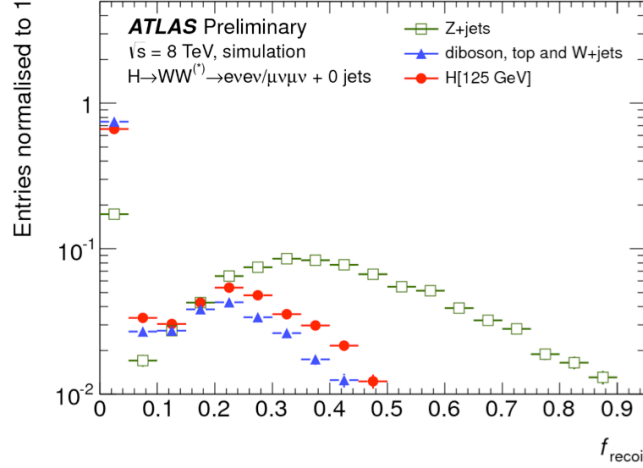gure 3.14 shows an early attempt to optimize the combination of the two cuts in the gluon fusion zero jet bin. Each bin shows the expected signal significance if the $p_\text{T,rel}^\text{miss (trk)}$ is required to be greater than the left edge of the bin and the f_recoil is required to be less than the top edge of the bin. The figure shows that the best signal significance comes from requiring low values of f_recoil (< 0.05) and $p_\text{T,rel}^\text{miss (trk)}$ values greater than 45 GeV.

3.6   Parameters of interest and statistical treatment

As with any search or measurement, there are particular parameters of the Higgs that the $H \to WW^*$ analysis is interested in measuring. In this case, the parameters of interest are the mass of the Higgs boson and its production cross section. Because the $H \to WW^* \to \ell\nu\ell\nu$ process does not have a closed final state, it is not possible to measure the full invariant mass of the particle that may have produced
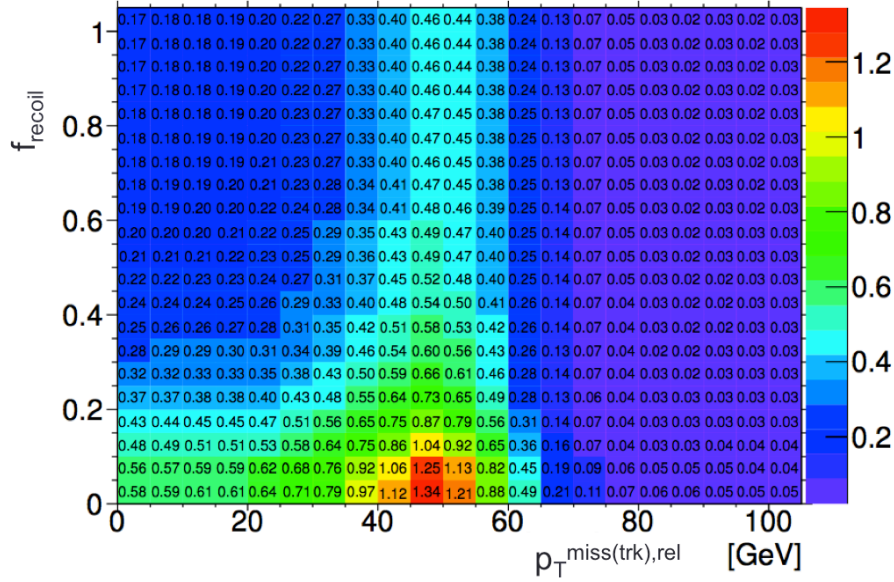
Figure 3.14: Signal significance as a function of cut value in the ggF $H \to WW^*$ with $n_j = 0$

the final state. However, a proxy for the invariant mass using transverse plane information can be defined. This is described in more detail in section 3.6.1. The second parameter of interest is the ratio of the measured cross section to that expected from the Standard Model Higgs, which is denoted a μ. This is defined in equation 3.5.

$$\mu = \frac{\sigma}{\sigma_{\mathrm{SM}}} \qquad (3.5)$$

All of the likelihoods used in the statistical analysis of the final signal region events are paramaterized as a function of μ. μ is a natural variable for hypothesis testing, as $\mu = 0$ corresponds to a background only hypothesis and $\mu = 1$ corresponds exactly to a Standard Model Higgs.

3.6.1 TRANSVERSE MASS

Because the longitudinal information about the neutrinos is not attainable, the $H \to WW^* \to \ell\nu\ell\nu$ analysis uses a mass variable, the transverse mass, that exploits information in the transverse plane as a

proxy for the full invariant mass. The transverse mass is defined in equation 3.6.

$$m_{\mathrm{T}} = \sqrt{\left(E_{\mathrm{T}}^{\ell\ell} + p_{\mathrm{T}}^{\mathrm{miss}}\right)^2 - \left|\, \boldsymbol{p}_{\mathrm{T}}^{\ell\ell} + \boldsymbol{p}_{\mathrm{T}}^{\mathrm{miss}} \,\right|^2},\tag{3.6}$$

Here the $E_{\mathrm{T}}^{\ell\ell}$ and $p_{\mathrm{T}}^{\ell\ell}$ are the transverse energy and momentum of the dilepton system, while $p_{\mathrm{T}}^{\mathrm{miss}}$ is a proxy for the transverse momentum of the di-neutrino system. The track-based $p_{\mathrm{T}}^{\mathrm{miss}}$ is used in the m_{T} rather than the calorimeter based $E_{\mathrm{T}}^{\mathrm{miss}}$ because it has a better resolution on the true transverse mass. Figure 3.12b shows the improvement in the RMS of the difference between the true and reconstructed transverse mass in a ggF signal sample. The RMS improves by 4.7 GeV using $p_{\mathrm{T}}^{\mathrm{miss}}$ in the m_{T} calculation.

3.6.2   Statistical treatment[*]

Likelihood function

The statistical analysis of final event candidates is framed as a hypothesis test, where the null hypothesis is background-only (no Standard Model Higgs). The first step in the analysis is to form a likelihood function for the data. In its simplest form, this likelihood is the probability of observing the number of events seen in the final signal region given knowledge of the signal strength. Because observation of events is fundamentally a Poisson counting experiment, this simple likelihood can be expressed as a Poisson probability of observing N events given a total number of predicted signal and background events. This basic likelihood is shown in equation 3.7.

$$\mathcal{L}(\mu) = P\left(N|\mu S + B\right)\tag{3.7}$$

Here, P is the Poisson probability density function, N is the total number of observed events, μ is the signal strength, S is the predicted number of signal events, and B is the predicted number of background events.

In particle physics, certain background estimates are commonly normalized in so-called "control" re-

---

[*]Many thanks to Aaron Armbruster, whose thesis[1] inspired parts of this section.

gions and those predictions are scaled by the same normalization factor in the signal region. This leads to a slightly more complicated likelihood, which is a function of both the signal strength and the background normalization. This is shown in equation 3.8.

$$\mathcal{L}(\mu, \theta) = P\left(N | \mu S + \theta B\right) P\left(N_{\mathrm{CR}} | \theta B_{\mathrm{CR}}\right) \tag{3.8}$$

Here, θ is a so-called "nuisance parameter", a parameter that is not a primary parameter of interest but still enters the likelihood. The second Poisson term adds an extra term to the likelihood, enforcing the fact that the background normalization must be consistent with the number of observed events in data in the control region, N_{CR}.

So far, these two formulations of likelihoods have assumed a single signal region and do not take into account any shape information of potential discriminating variables. The $H \to WW^*$ analysis is divided into many different categories, and we can perform the same counting experiment described above in each individual category. As mentioned in section 3.6.1, the transverse mass is used as the primary discriminating variable in many of the $H \to WW^*$ sub-analyses, so additionally we can perform the same counting experiment in each bin of the m_{T} distribution to incorporate some shape information. Thus, the total likelihood becomes a product over signal regions and bins of the m_{T} distribution. Finally, there are usually many backgrounds that are normalized in control regions, so the new formulation of the likelihood takes this into account as well by including a product over control regions in the second Poisson term. All of these modifications are shown in equation 3.9.

$$\mathcal{L}(\mu, \boldsymbol{\theta}) = \prod_{\substack{\mathrm{SRs\,i} \\ \mathrm{bins\,b}}} P\left(N_{ib} \middle| \mu S_{ib} + \sum_{\mathrm{bkg\,k}} \theta_k B_{kib}\right) \prod_{\mathrm{CRs\,l}} P\left(N_l \middle| \sum_{\mathrm{bkg\,k}} \theta_k B_{kl}\right) \tag{3.9}$$

The final step to get the full likelihood used in the analysis is to add nuisance parameters for the systematic uncertainties. In cases where the uncertainty does not affect the shape of m_{T} bin-by-bin, each systematic uncertainty ϵ is allowed to affect the expected event yields through a linear response function of the nuisance parameter, namely $\nu(\theta) = (1 + \epsilon)^\theta$. If instead the uncertainty does affect the shape, the effect is instead parameterized by $\nu_b(\theta) = 1 + \epsilon_b \theta$. The value of the nuisance parameters for the

systematic uncertainty are constrained with a Gaussian term that is added to the likelihood as well. This is of the form $g(\delta|\theta) = e^{-(\delta-\theta)^2/2}/\sqrt{2\pi}$, where δ is the central value and θ is a nuisance parameter. Finally, a last term is added to account for the statistical uncertainty in the Monte Carlo samples used, which adds an additional poisson term. The full likelihood used in the final statistical analysis is defined in equation 3.10.

$$
\begin{aligned}
\mathcal{L}\left(\mu, \boldsymbol{\theta}\right) = \prod_{\substack{\text{SRs i} \\ \text{bins b}}} P &\left(N_{ib} \middle| \mu S_{ib} \cdot \prod_{\substack{\text{sig.} \\ \text{syst.} \\ r}} \nu_{br}(\theta_r) + \sum_{\text{bkg k}} \theta_k B_{kib} \cdot \prod_{\substack{\text{bkg.} \\ \text{syst.} \\ s}} \nu_{bs}(\theta_s) \right) \\
&\cdot \prod_{\text{CRs l}} P \left(N_l \middle| \sum_{\text{bkg k}} \theta_k B_{kl} \right) \\
&\cdot \prod_{\substack{\text{syst} \\ t}} g\left(\delta_t|\theta_t\right) \cdot \prod_{\text{bkg k}} P\left(\xi_k|\zeta_k\theta_k\right)
\end{aligned}
\tag{3.10}
$$

In the fourth term of the equation, quantifying uncertainty due to finite Monte Carlo sample size, ξ represents the central value of the background prediction, θ is the associated nuisance parameter, $\zeta = (B/\delta B)^2$, where δB is the statistical uncertainty of B.

The best fit value of the signal strength μ is determined by finding the values of μ and $\boldsymbol{\theta}$ that maximize the likelihood, while setting $\delta = 0$ and $\xi = \zeta$.

Once the likelihood is defined, a test statistic must be built for use in hypothesis testing.

Test statistic

To distinguish whether the data match a background only or background and signal hypothesis, a test statistic must be used. The $H \rightarrow WW^*$ analysis used the profile likelihood technique[3]. The first step in formulating this test statistic is to define the profile likelihood ratio, shown in equation 3.11.

$$
\lambda(\mu) = \frac{\mathcal{L}\left(\mu, \hat{\hat{\theta}}_\mu\right)}{\mathcal{L}\left(\hat{\mu}, \hat{\theta}\right)}
\tag{3.11}
$$

Here $\hat{\hat{\theta}}_\mu$ is the value of θ that maximizes the likelihood for the choice of μ being tested. Additionally,

$\hat{\theta}$ and $\hat{\mu}$ represent the values of θ and μ that gives the overall maximum value of the likelihood.

Once this is defined, a test statistic q_μ is constructed. This is shown in equation 3.12.

$$q_\mu = -2 \ln \lambda(\mu) \tag{3.12}$$

A higher value of q_μ means that the data are more incompatible with the hypothesized value of μ, and q_0 then corresponds to the value of the test statistic for the background only hypothesis. A p_0 value is then defined to quantify the compatibility between the data and the null hypothesis. The p_0 value is the probability of obtaining a value of q_0 larger than the observed value, and this is shown in equation 3.13.

$$p_0 = \int_{q_0^{\text{obs}}}^{\infty} f(q_\mu | \mu = 0) dq_\mu \tag{3.13}$$

Here $f(q_\mu)$ is the probability distribution function of the test statistic. Finally, the p_0 value can be converted into a signal significance, using the formula in equation3.14, or the one-sided tail of the Gaussian distribution.

$$Z_0 = \sqrt{2} \text{erf}^{-1}(1 - 2p_0) \tag{3.14}$$

The threshold for discovery used in particle physics is $Z_0 \geq 5$, more commonly known as a value of 5σ.

4

The discovery of the Higgs boson and the

role of the $H \rightarrow WW^* \rightarrow \ell\nu\ell\nu$ channel

5

Observation of Vector Boson Fusion production of $H \rightarrow WW^* \rightarrow \ell\nu\ell\nu$

6

Combined Run 1 $H \to WW^* \to \ell\nu\ell\nu$ results

Part III

Search for Higgs pair production in the $HH \rightarrow b\bar{b}b\bar{b}$ channel in LHC Run 2 at $\sqrt{s} = 13$ TeV

7

Search overview

8

Search for Higgs pair production in boosted final states

9

Results with Run 2 2015 dataset

Part IV

Looking ahead

10
Conclusion

We found the Higgs. Then measured it. Then used it to look for new physics. What a time to be alive!

References

[1] Armbruster, A. J. (2013). Discovery of a higgs boson with the atlas detector. *CERN-THESIS-2013-047*.

[2] Collaboration, A. (2015). Observation and measurement of higgs boson decays to ww* with the atlas detector. *Phys. Rev. D*, 92(012006).

[3] G. Cowan, K. Cranmer, E. Gross, and O. Vitells (2011). Asymptotic formulae for likelihood-based tests of new physics. *Eur. Phys. J.*, C 71, 1554.

T HIS THESIS WAS TYPESET using LaTeX, originally developed by Leslie Lamport and based on Donald Knuth's TeX. The body text is set in 11 point Egenolff-Berner Garamond, a revival of Claude Garamont's humanist typeface. The above illustration, *Science Experiment 02*, was created by Ben Schlitter and released under CC BY-NC-ND 3.0. A template that can be used to format a PhD dissertation with this look & feel has been released under the permissive AGPL license, and can be found online at github.com/asm-products/Dissertate or from its lead author, Jordan Suchow, at suchow@post.harvard.edu.